IEEE Photonics Journal
An IEEE Photonics Society Publication

Open Access

Physical Mechanism and Response Characteristics of Unsaturated Optical Stopping-Based Amorphous Arsenic Sulfide Thin-Film Waveguides

Volume 11, Number 1, February 2019

Zhi Chen
Guande Wang
Xiong Wang, *Member, IEEE*

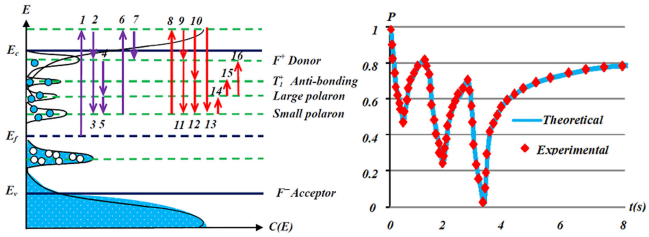

DOI: 10.1109/JPHOT.2019.2894741
1943-0655

Physical Mechanism and Response Characteristics of Unsaturated Optical Stopping-Based Amorphous Arsenic Sulfide Thin-Film Waveguides

Zhi Chen,[1] **Guande Wang**,[2] **and Xiong Wang**,[1] ***Member, IEEE***

[1]School of Information Science and Technology, ShanghaiTech University, Shanghai 200031, China
[2]State Key Laboratory of High Field Laser Physics, Shanghai Institute of Optics and Fine Mechanics, Chinese Academy of Sciences, Shanghai 201800, China

DOI:10.1109/JPHOT.2019.2894741

Manuscript received December 19, 2018; revised January 15, 2019; accepted January 16, 2019. Date of publication January 31, 2019; date of current version February 8, 2019. This work was supported by the National Natural Science Foundation of China (NSFC) under Grant 61701305. (Zhi Chen and Guande Wang contributed equally to this work.) Corresponding authors: Guande Wang and Xiong Wang (e-mail: wgd@siom.ac.cn; wangxiong@shanghaitech.edu.cn).

Abstract: Optical stopping can serve as a light-controlled solution to implementing photonic components. In contrast to saturated optical stopping that provides enough excited electrons to entirely absorb signal lights, unsaturated optical stopping introduces a photon competition mechanism for signal lights and pump lights due to insufficient excited electrons. This photon competition mechanism produces a kind of regular signals, which is very similar to the signals applied in pulse-coupled neural network. However, due to its unclear physical mechanism, it is impossible to further improve performances of the unsaturated optical stopping-based components. Here, we propose a kinetic model to reveal physical mechanism of the unsaturated optical stopping and establish a corresponding formalism that enables calculation of time response of the unsaturated optical stopping-based amorphous arsenic sulfide thin-film waveguides. Our work provides a new insight into the physical phenomenon of unsaturated optical stopping and builds a theoretical foundation for further research on response characteristics of amorphous arsenic sulfide thin-film waveguides.

Index Terms: Unsaturated optical stopping, physical mechanism, response characteristics, optical waveguides, pulse-coupled neural network.

1. Introduction

Chalcogenide glasses possess attractive optical properties [1]–[6], which is of significant meaning to optoelectronics and photonics [7]–[14]. A prominent advantage of some chalcogenide glasses is that their photoelectric characteristics can be flexibly tailored by adjusting stoichiometric composition [15]. Arsenic sulfide (As_2S_8) is a typical kind of such composition-adjustable chalcogenide glasses, contributing significantly to fabrication of optical fibers and waveguides [16]–[23] utilized in optoelectronics, photonics and metamaterials [24]–[27]. Average coordination number of the As_2S_8 is relatively low while its defect density in chemical bonds is relatively high, leading to more sublevels in the bandgap of this material. Due to photon absorption by the electrons in the sublevels, some unique optical phenomenon including optical stopping has been observed [28]–[31]. To enable the

occurrence of optical stopping, thin-film waveguides formed by As_2S_8 or its doped materials are indispensable [29], [30], which have been studied extensively in terms of phenomenon [29], [30], mechanism [31], and applications [32]. Understanding underlying physics of the optical stopping is very beneficial for improving performances and developing novel photonic components. However, previous work only concentrated on recovery segments in the optical stopping to lift its respond time [31] and hardly emphasized the physical mechanism of the whole process of the optical stopping. Besides, it is far from being sufficient for the unsaturated optical stopping to only understand recovery segments in the whole process. In addition, while the saturated optical stopping can only serve as a function of switch, the unsaturated optical stopping behaves as a process of regularly accumulation and release of signal energies, which is very similar to the mechanism of Pulse-Coupled Neural Network (PCNN) that is a kind of artificial intelligence (AI) [33]–[35]. Therefore, it is particularly necessary to research on the physical mechanism and to analyze the response characteristics of the unsaturated optical stopping.

In contrast to saturated optical stopping, unsaturated optical stopping cannot provide enough excited electrons that entirely absorb photons of a signal light, leading to competition between photons of signal lights and pump lights. This is because the physical mechanism of the unsaturated optical stopping is intrinsically different from that of the saturated optical stopping. While almost all previous work focuses on saturated optical stopping, little effort has been devoted to investigating the unsaturated optical stopping. Given that the unsaturated optical stopping holds potential for novel optical components, it is highly meaningful to conduct further comprehensive research on the mechanism of the unsaturated optical stopping. Furthermore, the unsaturated optical stopping can be applied in generation of pulsed optical signals with adjustable intensity, providing a novel method to implement optical signal generators especially in PCNN. Such promising application prospects stimulate us to establish the kinetic model for the unsaturated optical stopping. On the basis of both hybrid orbital and electron energy bandgap theory, the kinetic model is proposed and analyzed in this work. The response time of the unsaturated optical stopping-based components can be faithfully predicted by the proposed formalism, which is validated by very good accordance between theoretical work and experimental data.

2. Experimental Observation of Unsaturated Optical Stopping

Optical stopping is a phenomenon in which a signal light can be quenched by a pump light in waveguides made of As_2S_8 or its doped materials like tin arsenic sulfide (Sn-As-S). In practice, a 442-nm He-Cd laser is often used for the pump light, while a 633-nm He-Ne laser serves as the signal light. An interesting feature of the optical stopping is that the intensity of the signal light regularly varies with time, producing an optical switch in the condition of the saturated optical stopping or an optically controlled signal generator in the case of the unsaturated optical stopping. The latter could be more meaningful as a neuron component in the PNCC and its mechanism consequently deserves much research.

Experiment setup shown in Fig. 1 is established to observe the unsaturated optical stopping. A thin-film waveguide is comprised of a Sn-As-S core layer and quartz substrates. The refractive index of Sn-As-S core and quartz substrates are 2.2988 and 1.457 at the wavelength of 633-nm, respectively. To form such a thin-film waveguide, it is easy to deposit Sn-As-S glass powder on the quartz substrates by vacuum evaporation. The thickness of the Sn-As-S core layer can be controlled by the weight of deposited Sn-As-S and measured by prism coupling. In this work, the thickness of the Sn-As-S core layer is 500-nm. The length and the width of the Sn-As-S core layer are both as the same as those of substrates. The length, width and height of the substrates are 60-mm, 10-mm, and 1-mm, respectively. A randomly polarized incident light with the power of 2-mW from a 633-nm laser source is transformed to a linearly polarized light by a polarizer, spatially filtered by an aperture, and focused on a prism. The prism couples the signal light into a Sn-As-S thin-film waveguide, while another prism is employed to guide the signal light out of the waveguide. A pump light from a 442-nm He-Cd laser source is controlled by an optical switch (OS) to irradiate the signal light in the Sn-As-S thin-film waveguide via a coupling fiber, resulting in variation of intensity of

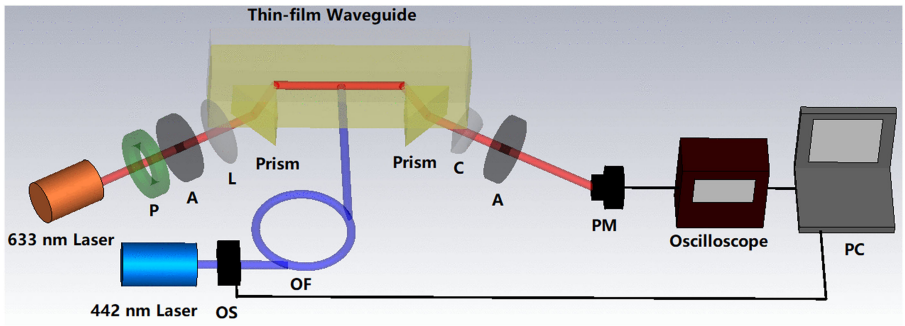

Fig. 1. Experimental setup for unsaturated optical stopping in a Sn-As-S thin-film waveguide. OS, Optical Switch; OF, Optical Fiber; P, Polarizer; A, Aperture; L, Lens; C, Cylinder Lens; PM, Power Meter.

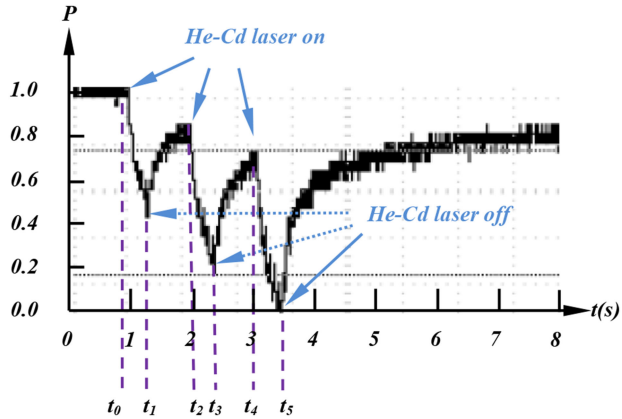

Fig. 2. Power curve of signal light as a function of time in the process of unsaturated optical stopping, which is captured by an oscilloscope. (A He-Cd laser source provides the 442-nm pump light. *P* represents the power of the 633-nm laser.)

the outgoing signal light. The irradiation power of the pump light is 12.5-mW and the irradiation light radius is 1.5-mm. The outgoing light is focused by a cylinder lens, filtered by an aperture, and finally detected by a power meter. An oscilloscope records electrical signals obtained by the power meter. Generally, a voltage curve displayed on the oscilloscope is a straight line if the 633-nm laser source provides continue wave (CW) and the 442-nm laser source is shut down. However, with the pump light turned on, the voltage drops to nearly zero. In other words, the signal light cannot be observed, with the pump light irradiating the propagation path of the signal light in the waveguide. This phenomenon is referred to as the optical stopping. If an OS converts the CW pump light into a pulsed pump light with proper time interval, the recorded voltage exhibits oscillatory behavior and gradually decreases, as shown in Fig. 2.

The voltage curve is essentially the time response of an amorphous arsenic sulfide thin-film waveguide involving the unsaturated optical stopping. To facilitate the analysis of the unsaturated optical stopping, its entire process is divided into a number of segments in time domain that can be classified into two categories, one is blocking segment (from t_0 to t_1, from t_2 to t_3, and from t_4 to t_5), and the other is recovery segment (from t_1 to t_2, from t_3 to t_4, and from t_5 to infinity).

3. Kinetic Model for Unsaturated Optical Stopping

Here, the optical stopping is considered as a result of electron transition among different energy bands [29], [31]. Amorphous As_2S_8 has lots of defect states in chemical bonds due to its anomalous

electron configurations. These under and over coordinated defects introduce a special bandgap structure, making the optical stopping possible.

As electron configuration of the outermost layer of an arsenic atom (As) is s^2p^3, its normal bond state ($A\,s_3^0$) has three degree coordination and three unpaired p bonding electrons. Correspondingly, normal bond state (S_2^0) of a sulphur atom (S) has two degree coordination and two unpaired p bonding electrons owing to its s^2p^4 electron configuration in the outermost layer. Therefore, a molar ratio of 2:3 is ideal for the coordination of arsenic sulfur compounds and a corresponding material is As_2S_3. However, if a molar ratio of 2:8 is applied to form arsenic sulfur compounds, a corresponding material is not As_2S_3 but As_2S_8. As_2S_8 possesses lots of chemical bond defects including anti-bond and dangling-bond due to insufficient and over coordination. Since high-energy electrons in anti-bond and dangling-bond are unstable, they tend to interact with adjacent electrons in normal-bond, inducing new defect states. This transition reduces lattice energy, releases heat, and provides negative effective correlation energy. Besides, lattice distortion and atomic relaxation take place in the transition as well. Some expressions are employed to describe the transition of states, which are $S_2^0 + S_1^0 \rightarrow S_2^0 + S_3^0$, $2S_3^0 \rightarrow S_3^+ + S_1^-$, $A\,s_3^0 + A\,s_2^0 \rightarrow A\,s_3^0 + A\,s_4^0$, and $2A\,s_4^0 \rightarrow A\,s_4^+ + A\,s_2^-$. Here, S_1^0 and $A\,s_2^0$ are both dangling-bond defect states in an S and an As, respectively. Owing to instability, anti-bonding electrons in one S_3^0 could transfer to another S_3^0, rendering one S_3^0 becomes S_3^+ and the other S_3^0 become S_1^-. The defect state $A\,s_4^0$ has the similar effect as S_3^0. Ultimately, As_2S_8 contains the primary defect state S_3^+ and S_1^- in the S atoms, while $A\,s_4^+$ and $A\,s_2^-$ in the As atom. S_3^+ and $A\,s_4^+$ offer three and four hybrid electrons (sp^3), respectively. S_1^- and $A\,s_2^-$ provide one and two p electrons, respectively. The electrons in these primary defect states tend to form valence-alternation pairs (VAPs) at a lower energy level. The VAP obeys Coulomb effect that can be explained as the lager the Coulombic force, the closer the distance between electrons. Consequently, some electrons close enough tend to form intimate valence-alternation pairs (IVAPs), lowering down the energy of the whole structure. In As_2S_8, the concentration of IVAPs is higher than that of VAPs. In addition, the mole number of As_2S_8 is dominated by S so that the ruling type of defect state is $S_3^+ - S_1^-$. To classify the defect states, S_3^+ and $A\,s_4^+$ are represented by F^+, S_1^- and $A\,s_2^-$ are represented by F^-, and S_3^0, S_1^0, $A\,s_4^0$ and $A\,s_2^0$ are represented by F^0. F^+-F^- corresponds to loose-binding exciton in VAPs, while tight-binding exciton in IVAPs. These excitons interact with excited electrons, forming large polarons and small polarons. Electrons in shallow energy gap are inclined to be captured by the large polaron potential wells, while electrons in deep energy gap are prone to be captured by the small polaron potential wells.

In general, some impurity elements involved in As_2S_8 is beneficial to improve optical stopping [29]. Take Sn as an example, the electron configuration of the outermost layer of a tin atom (Sn) is s^2p^2 that provides 4 electrons and transforms into sp^3 in normal compound reactions. Since electronegativity of Sn (1.8) is smaller than that of S (2.5), electrons in the coordination bond formed by Sn and S are close to S and Sn thus shows ionicity. In addition, the atomic radius of Sn (0.141 nm) is larger than that of As (0.125 nm), making the bond intension of Sn-S smaller than that of As-S. Furthermore, the absorption edge of Sn (1 eV) is smaller than that of As (2 eV) and S (2.5 eV). All those factors induce the band gap of Sn-As-S to be narrower than As-S, rendering polaron potential wells shallower and producing the anti-bonding energy level.

The optical stopping is a result of electron transition among flawed energy bands [31]. The variation of the concentration of the self-trapped electrons with time is a typical microscopic physical feature of the optical stopping and can be utilized to quantitatively describe the process of the optical stopping [29], [31]. In contrast to the saturated optical stopping having only one cycle period, the electron transition process for the unsaturated optical stopping has many cycle periods and every cycle period mainly consist of 16 steps as shown in Fig. 3. E_c represents mobility edge of conduction band, while E_v indicates mobility edge of valence band. $C(E)$ denotes concentration of states. The electron transition process is described in details as followings.

Step 1: as a He-Cd laser irradiates a Sn-As-S thin-film waveguide, electrons in the F^- are excited to the extended state above E_c via absorption of photon energy of the 442-nm laser and F^- is converted into F^0.

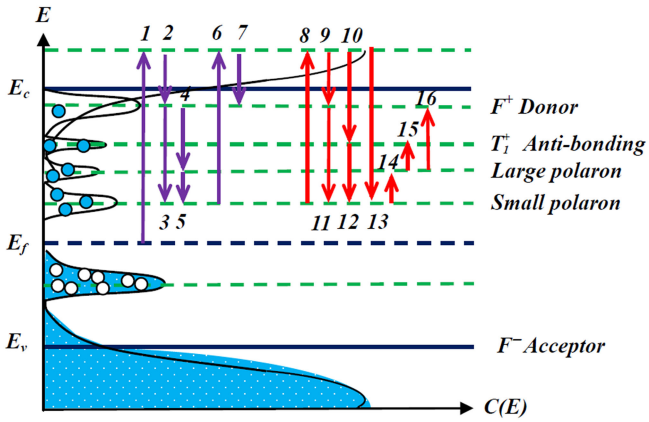

Fig. 3. Kinetic model for unsaturated optical stopping in amorphous arsenic sulfide thin-film waveguides.

Step 2: the excited electrons in the extended state are trapped by F^+ via atomic relaxation, consequently falling into the tail of the conduction band. The electrons in the tail of the conduction band are unstable, resulting in two types of potential interactions between the electrons and $F^+ - F^-$.

Step 3: one type of interaction is the Coulomb interaction that induces local lattice distortion, decreases electronic electrostatic potential in the local region, and produces small polaron potential wells that are capable of trapping electrons.

Step 4: the other type of interaction is the mutual effect, leading to formation of large polaron potential wells.

Step 5: however, the loose-binding self-trapped electrons in the large polarons are unstable. They are likely to interact with tight-binding excitons via Coulomb interaction, resulting in new small polaron potential wells.

The procedure from Step 1 to Step 5 represents the segment of He-Cd laser pumping, in which self-trapped electrons in the small polarons indeed increase, offering a quantized foundation for optical stopping.

Step 6: as the 633-nm laser propagates thorough the Sn-As-S thin-film waveguide, the self-trapped electrons in the polarons absorb photons of 633-nm laser and are subsequently excited to the extended state above E_c. The overall effect in this step exhibits signal light blocking in a macroscopic level.

Step 7: the excited electrons in the extended state are trapped by F^+ via atomic relaxation, consequently falling into the tail of the conduction band. Due to almost full of electrons in the polaron potential wells via continuous pumping by He-Cd laser, the electrons in the tail of the conduction band have hardly opportunity to enter into the polaron potential wells while to be combined with F^+ to form F^0. One F^0 interacts with adjacent F^0, leading to an exothermic reaction ($2F^0 \rightarrow F^+ + F^-$), deexcitation and compensation of F^+-F^-.

The procedure from Step 1 to Step 7 constitutes the entire segments of blocking. As the He-Cd laser continuously irradiates the Sn-As-S thin-film waveguide, an endless supply of electrons are pumped into small polaron potential wells and the optical blocking is thus sustained.

Step 8: at the time that the He-Cd laser is turned off, many polaron potential wells are still occupied by electrons that could absorb photons of the 633-nm laser and are subsequently excited to the extended state above E_c. The electrons in the extended state could be trapped by tow potential defect states via atomic relaxation.

Step 9: some excited electrons are trapped by F^+ resulting in F^0.

Step 10: other excited electrons are absorbed by T_1^+ , forming anti-bonding potential wells, where T_1^+ is an anti-bonding defect state provided by Sn atoms.

Step 8, Step 9 and Step 10 constitute the former fast procedure in the recovery segment. In the next moment, with self-trapped electrons in polaron potential wells decreasing, the relative high energy electrons in three different energy levels are more likely to be trapped by the polaron potential wells.

Step 11: electrons in the F^+ energy level are trapped by the polaron potential wells.

Step 12: electrons in the T_1^+ energy level are trapped by the polaron potential wells.

Step 13: electrons in the extended state above E_c are trapped by the polaron potential wells. Since electrons from both the F^+ energy level and the extended state above E_c are hijacked by T_1^+, the recovery speed of the electron concentration in the polaron potential wells slows down.

Step 14: conversely, electrons in the small polaron potential wells could absorb heat so as to jump back to the large polaron potential wells. The electrons in the large polaron potential wells are unstable and could transfer into two potential energy levels by absorbing heat.

Step 15: one possibility is transition into F^+ energy level.

Step 16: the other possibility is transition into T_1^+ energy level.

The procedure from Step 11 to Step 16 repeatedly run for several times, showing the latter slow procedure in the recovery segment. Ultimately, the pumping rate of the electrons in the polaron potential wells is the same as their filling rate and the phenomenon of the optical stopping disappears.

Basically, the motivator of the transmission recovery of the signal light is caused by the decrement in electrons in the small polaron potential wells, while the driving force for the increment of electrons in the small polaron potential wells is derived from the pumping effect by the He-Cd laser. Therefore, providing that He-Cd laser pumps once more, electrons in the small polaron potential wells increase again as the same situation as the Step 1 and the He-Ne laser is subsequently blocked again. What needs to be emphasized is that the process of the electron transition in the unsaturated optical stopping is more complicated than that of the saturated optical stopping. The 16 steps aforementioned entirely describe the saturated optical stopping, whereas it really needs more than 16 steps to present the unsaturated optical stopping. More importantly, the concentration of self-trapped electrons in the small polaron potential wells is zero at the moment of the first pumping by using 442-nm lasers, while that will be some certain value at the moment of the second and subsequent pumping. Such existing self-trapped electrons induce a photon competitive mechanism between the 633-nm laser and the 442-nm laser, which is a distinctive feature for the unsaturated optical stopping and lays a foundation for controllability of the unsaturated optical stopping.

4. Formalism and Analysis

Based on our model, the unsaturated optical stopping can be characterized as change in concentration of self-trapped electrons in the small polaron potential wells with time [31]. In the blocking segment, as the He-Cd laser irradiates the Sn-As-S thin-film waveguide for the first time, electrons are beginning to be pumped and transit among energy bands, meaning that the trigger of unsaturated optical stopping is pressed. The pumped electrons will go through some processes, inducing remarkable change in number of self-trapped electrons in the small polaron potential wells. As presented as the procedure form Step 1 to Step 7 in the Part 3, the change in the concentration depends on the 442-nm laser pumping, exciton recombination driven by heat balance, the 633-nm laser pumping, and high-energy level electronics trapped by the small polaron potential wells, which can be expressed as

$$dC = N_p \varphi_p \mu_p \left(C - C^2/C_{\max}\right) dt - \varepsilon C^2 dt - N_s \varphi_s \mu_s C dt + \psi N_s \varphi_s \mu_s C dt \tag{1}$$

where C is the concentration of self-trapped electrons in the small polaron potential wells, t is time, N_p is the number of photons of the 442-nm laser per unit time per unit area, φ_p is the quantum yield of the 442-nm laser, $\mu_p(C - C^2/C_{\max})$ is the effective absorption coefficient, μ_p is the absorption area of the 442-nm photons, $C_{\max}$ is the maximum tolerance of the concentrated self-trapped electrons in the small polaron potential wells, ϵ is the recombination probability coefficient, N_s is the number

of photons of the 633-nm laser per unit time per unit area, μ_s is the absorption area of the 633-nm photons, φ_s is the quantum yield of the 633-nm laser, $\psi$is a dimensionless ratio factor and named as recapture coefficient. By solving Eq. (1) and normalizing the solution, the time response for blocking process can be expressed as

$$1-\frac{C}{C_\infty}=\frac{\frac{2}{k_{sl}}\exp\left(-\frac{t}{2k_{sl}}\right)}{\left(\frac{1}{k_{sl}}+\frac{1}{k_l}\right)\exp\left(\frac{t}{2k_{sl}}\right)+\left(\frac{1}{k_{sl}}-\frac{1}{k_l}\right)\exp\left(-\frac{t}{2k_{sl}}\right)} \tag{2}$$

where $C_\infty = 2N_p\mu_p\varphi_p k_{sl}k_l/(k_{sl}+k_l)$, $1/k_{sl}=[(1/k_l)^2+4N_p\mu_p\varphi_p\varepsilon]^{1/2}$, and $1/k_l=(1-\psi)\,N_s\mu_s\varphi_s+N_p\mu_p\varphi_p/C_{\max}$. $1-C/C_\infty$ is the normalized expression of the power of the 633-nm lasers and can be represented as P. C_∞ is the saturated concentration of self-trapped electrons in the polaron potential wells as $t\to\infty$, proportional to N_p, k_l and k_{sl}. This is because the larger the k_l or k_{sl}, the longer effective life of self-trapped electrons in the small polaron potential wells. k_{sl} equals to k_l if deexcitation is not taken into account. $2k_{sl}$ is the effective life of self-trapped electrons in the small polaron potential wells. $N_p\mu_p\varphi_p\varepsilon$ is proportional to the number of deexcitation electrons excited by He-Cd laser and laying in self-trapped state in the small polaron potential wells. $(1-\psi)\,N_s\mu_s\varphi_s$ is proportional to the number of electrons excited from the self-trapped state in the small polaron potential wells to the extended state by He-Ne laser photons per unit volume per unit time. $N_p\mu_p\varphi_p/C_{\max}$ is inversely proportional to the maximum tolerance of the concentration of self-trapped electrons in the small polaron potential wells.

The recovery process of the unsaturated optical stopping can also be featured as change in concentration of self-trapped electrons in the small polaron potential wells with time. However, the time response for recovery process is asymmetric with the time response for blocking process and its normalized form can be represented as [31]

$$1-\frac{C}{C_0}=\frac{\left(1+\frac{k_1}{k_0}\right)\left[1-\exp\left(-\frac{t}{k_1}\right)\right]}{1+\frac{k_1}{k_0}\left[1-\exp\left(-\frac{t}{k_1}\right)\right]} \tag{3}$$

where C_0 is the concentration of self-trapped electrons in the small polaron potential wells at the moment when He-Cd laser is just cut off, $1/k_0$ is the recombination probability of self-trapped electrons in the small polaron potential wells and $1/k_0=\epsilon C_0$, and $1/k_1$ is the pumping rate of electrons excited from self-trapped state to extended state by He-Ne laser photons per unit time per unit volume and $1/k_1=(1-\psi)N_s\mu_s\varphi_s$. As the similar as Eq. (2), 1 - C/C_0 is also the normalized expression of the power of the 633-nm laser and can be represented as P.

In our formalism, k is related to both material parameters of Sn-As-S and laser parameters of the signal light and pumping light, such as absorption coefficient, quantum yield, absorption area, laser power, laser wavelength and so on. Although laser wavelength is not directly included in the formalism, some parameters have apparently quantitative relationship with laser wavelength, like absorption coefficient. This means all physical information can be expressed by the formalism. In addition, several thin-film waveguides with the same materials and different geometrical parameters were employed to implement the unsaturated optical stopping and their response features are much the same, which indicates geometrical parameters of the thin-film waveguides hardly impact performances of the unsaturated optical stopping and are not therefore included in the formalism. Here, curve fitting method is employed to obtain some appropriate k to validate the formalism. As shown in Fig. 2, the experimental curve captured by an oscilloscope is divided into some segments according to the blocking process and the recovery process. The curve for blocking process is fitted by using Eq. (2), while the curve for recovery process is fitted by using Eq. (3).

Good agreement between the theoretical curve and the experimental data is observed in Fig. 4, which undoubtedly corroborate the formalism. For ease of comparison with the experimental time responds curve in Fig. 2, the overall curve-fit of P is shown in Fig. 5. In addition, k is a highly important feature parameter for the time response of the Sn-As-S thin-film waveguide in the unsaturated optical stopping. k_{sl} and k_l are achieved via fitting by using Eq. (2), while k_0 is obtained

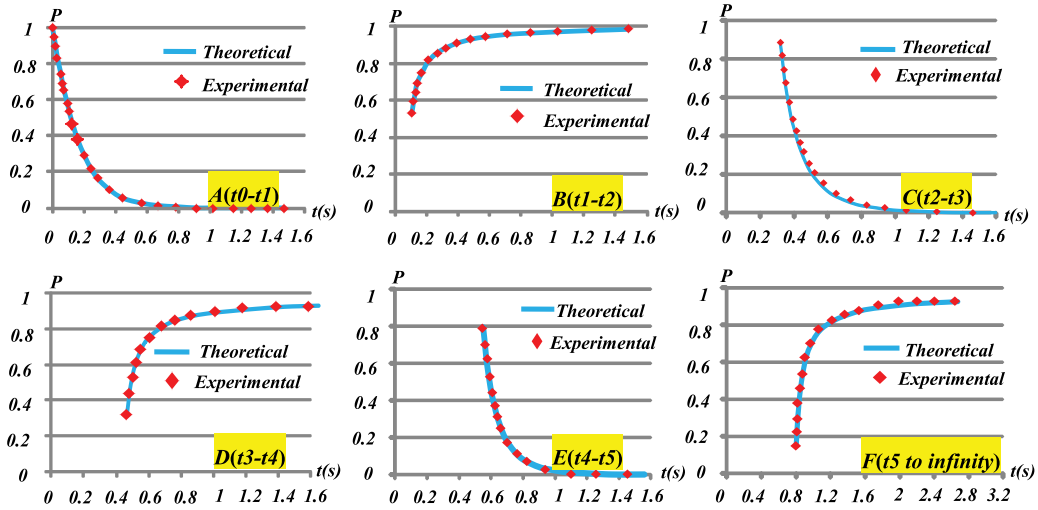

Fig. 4. Theoretical curve compared with experimental data. (P is the normalized power of 633-nm laser, t is time. The time response curves from A to F represent the procedures from t_0-t_1 to t_5-infinity. To achieve accurate results, we prolong the logging time of every segment and use such more data in the fitting.)

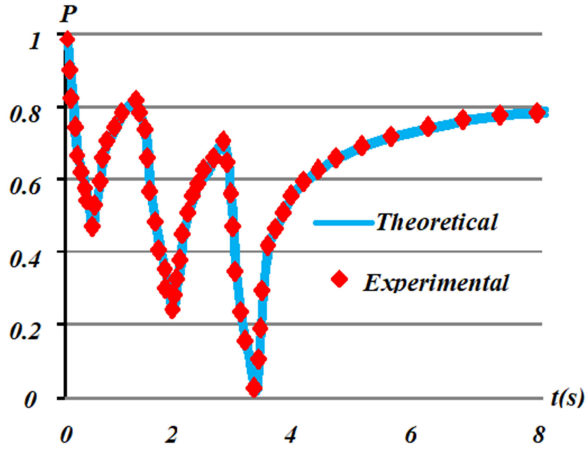

Fig. 5. Theoretically calculated time responds curve, compared with experimental data.

via fitting by using Eq. (3). In the first blocking segment as shown in Fig. 4 A, k_{sl} is 0.1429 and k_l is 0.1537. In the second blocking segment as shown in Fig. 4 C, k_{sl} is 0.1277 and k_l is 0.1382. In the third blocking segment as shown in Fig. 4 E, k_{sl} is 0.0789 and k_l is 0.0848. According to $k_{0i} = 1/\epsilon C(t_i)$, the life time of non-equilibrium carriers k_{0i} is not only associated with the recombination rate (ϵ) but also the concentration of the trapped electrons in the small polaron potential wells $C(t_i)$. Because the optical stopping is unsaturated, $C(t_i)$ is larger than the previous one in the beginning of the every blocking segment. As $C(t_i)$ becomes larger, k_{0i} decreases from $k_{01} = 0.0989$ in the segment of t_0-t_1 to $k_{03} = 0.0893$ in the segment of t_2-t_3, and then to $k_{05} = 0.0689$ in the segment of t_4-t_5. In the recovery segment, it is also indicated that k_{0i} decreases from $k_{02} = 19.6219$ in the segment of t_1-t_2 to $k_{04} = 14.3278$ in the segment of t_3-t_4. The respond characteristics of the unsaturated optical stopping depend obviously on the parameter k in the formalism, which provides an optimization method to improve respond characteristics by adjusting

k that is decided by both material parameters of Sn-As-S and laser parameters of the signal light and pump light.

5. Conclusion

In summary, we have built a kinetic model for response characteristics of unsaturated optical stopping-based amorphous arsenic sulfide thin-film waveguides. The electron transfer in the model is analyzed and as a foundation for establishing the formalism. The theoretical curve fitted by the formalism matches very well with the experimental data. The parameters and their corresponding relations in the formalism can express physical information in experiments with different conditions very well, which demonstrates the formalism has universality for such kind of thin-film waveguides. Our model provides a theoretical foundation for accurate prediction for the time response characteristics of amorphous arsenic sulfide film waveguides and paves a new way to investigate amorphous arsenic sulfide waveguide-based components. It is expected that highly performance amorphous arsenic sulfide film waveguides can be engineered via adjusting the parameters according to our formalism.

References

[1] S. Serna *et al.*, "Nonlinear optical properties of integrated GeSbS chalcogenide waveguides," *Photon. Res.*, vol. 6, pp. B37–B42, May 1, 2018.

[2] M. Micoulaut, A. Piarristeguy, H. Flores-Ruiz, and A. Pradel, "Towards accurate models for amorphous GeTe: Crucial effect of dispersive van der Waals corrections on the structural properties involved in the phase-change mechanism," *Phys. Rev. B*, vol. 96, Nov. 17, 2017, Art. no. 184204.

[3] T. V. Moreno *et al.*, "Potentiometric sensors with chalcogenide glasses as sensitive membranes: A short review," *J. Non-Crystalline Solids*, vol. 495, pp. 8–18, Sep. 1, 2018.

[4] Y. T. Xu *et al.*, "Improvement of the Faraday effect in Ge-S based chalcogenide glasses via gallium and lead compositional modifications," *Opt. Mater. Exp.*, vol. 8, pp. 1754–1761, Jul. 1, 2018.

[5] P. Boolchand, M. Bauchy, M. Micoulaut, and C. Yildirim, "Topological phases of chalcogenide glasses encoded in the melt dynamics," *Physica Status Solidi B, Basic Solid State Phys.*, vol. 255, Jun. 2018, Art. no. 1800027.

[6] M. Xie *et al.*, "Correlation among structure, water peak absorption, and femtosecond laser ablation properties of Ge-Sb-Se chalcogenide glasses," *J. Phys. Chem. C*, vol. 122, pp. 1681–1687, Jan. 25, 2018.

[7] H. T. Lin *et al.*, "Chalcogenide glass-on-graphene photonics," *Nature Photon.*, vol. 11, pp. 798–805, Dec. 2017.

[8] L. Li *et al.*, "High-performance flexible waveguide-integrated photodetectors," *Optica*, vol. 5, pp. 44–51, Jan. 20, 2018.

[9] L. Li *et al.*, "Integrated flexible chalcogenide glass photonic devices," *Nature Photon.*, vol. 8, pp. 643–649, Aug. 2014.

[10] N. Abdukerim, I. Alamgir, and M. Rochette, "All-fiber frequency-resolved optical gating pulse characterization from chalcogenide glass," *Opt. Lett.*, vol. 43, pp. 3228–3231, Jul. 15, 2018.

[11] V. Mittal, M. Nedeljkovic, D. J. Rowe, G. S. Murugan, and J. S. Wilkinson, "Chalcogenide glass waveguides with paper-based fluidics for mid-infrared absorption spectroscopy," *Opt. Lett.*, vol. 43, pp. 2913–2916, Jun. 15, 2018.

[12] M. R. Lotz, C. R. Petersen, C. Markos, O. Bang, M. H. Jakobsen, and R. Taboryski, "Direct nanoimprinting of moth-eye structures in chalcogenide glass for broadband antireflection in the mid-infrared," *Optica*, vol. 5, pp. 557–563, May 20, 2018.

[13] H. L. Butcher, D. G. MacLachlan, D. Lee, R. R. Thomson, and D. Weidmann, "Demonstration and characterization of ultrafast laser-inscribed mid-infrared waveguides in chalcogenide glass IG2," *Opt. Exp.*, vol. 26, pp. 10930–10943, Apr. 16, 2018.

[14] G. Y. Liu *et al.*, "Threshold switching in SiGeAsTeN chalcogenide glass prepared by As ion implantation into sputtered SiGeTeN film," *Appl. Phys. Lett.*, vol. 111, Dec. 18, 2017, Art. no. 252102.

[15] M. Mohamed, A. Y. Abdel-Latief, M. A. Abdel-Rahim, N. M. A. Hadia, E. R. Shaaban, and M. N. Abd-el Salam, "Examination of the kinetic reaction mechanisms of amorphous As50Se50 chalcogenide glass," *Appl. Phys. A, Mater. Sci. Process.*, vol. 124, pp. 562-1–562-9.

[16] C. Tsay, Y. L. Zha, and C. B. Arnold, "Solution-processed chalcogenide glass for integrated single-mode mid-infrared waveguides," *Opt. Exp.*, vol. 18, pp. 26744–26753, Dec. 6, 2010.

[17] X. Xia, Q. Chen, C. Tsay, C. B. Arnold, and C. K. Madsen, "Low-loss chalcogenide waveguides on lithium niobate for the mid-infrared," *Opt. Lett.*, vol. 35, pp. 3228–3230, Oct. 1, 2010.

[18] X. Gai *et al.*, "Progress in optical waveguides fabricated from chalcogenide glasses," *Opt. Exp.*, vol. 18, pp. 26635–26646, Dec. 6, 2010.

[19] A. P. Velmuzhov *et al.*, "Fiber sensor on the basis of Ge26As17Se25Te32 glass for FEWS analysis," *Opt. Mater.*, vol. 75, pp. 525–532, Jan. 2018.

[20] L. Zhang, W. C. Zhou, and A. Y. Yi, "Investigation of thermoforming mechanism and optical properties' change of chalcogenide glass in precision glass molding," *Appl. Opt.*, vol. 57, pp. 6358–6368, Aug. 1, 2018.

[21] J. Cui *et al.*, "Mid-infrared emissions of Dy^{3+} doped Ga-As-S chalcogenide glasses and fibers and their potential for a 4.2 μm fiber laser," *Opt. Mater. Exp.*, vol. 8, pp. 2089–2102, Aug. 1, 2018.

[22] Z. G. Xue *et al.*, "Infrared suspended-core fiber fabrication based on stacked chalcogenide glass extrusion," *J. Lightw. Technol.*, vol. 36, pp. 2416–2421, Jun. 15, 2018.
[23] Y. F. Zhai, R. D. Qi, C. Z. Yuan, W. Zhang, and Y. D. Huang, "High-quality chalcogenide glass waveguide fabrication by hot melt smoothing and micro-trench filling," *Appl. Phys. Exp.*, vol. 9, May 2016, Art. no. 052201.
[24] B. J. Eggleton, B. Luther-Davies, and K. Richardson, "Chalcogenide photonics," *Nature Photon.*, vol. 5, pp. 141–148, Mar. 2011.
[25] J. J. Hu *et al.*, "Resonant cavity-enhanced photosensitivity in As2S3 chalcogenide glass at 1550 nm telecommunication wavelength," *Opt. Lett.*, vol. 35, pp. 874–876, Mar. 15, 2010.
[26] D. Conteduca, F. Dell'Olio, C. Ciminelli, and M. N. Armenise, "New miniaturized exhaled nitric oxide sensor based on a high Q/V mid-infrared 1D photonic crystal cavity," *Appl. Opt.*, vol. 54, pp. 2208–2217, Mar. 20, 2015.
[27] Q. B. Jiang *et al.*, "Metasurface for reciprocal spin-orbit coupling of light on waveguiding structures," *Phys. Rev. Appl.*, vol. 10, Jul. 17, 2018, Art. no. 014014.
[28] M. Shpotyuk, A. Kovalskiy, R. Golovchak, and O. Shpotyuk, "Phenomenology of gamma-irradiation-induced changes in optical properties of chalcogenide semiconductor glasses: A case study of binary arsenic sulfides," *J. Non-Crystalline Solids*, vol. 498, pp. 315–322, Oct. 15, 2018.
[29] L. P. Du *et al.*, "Optical stopping effect of impurity-doping As2S8 glass waveguide," *Acta Physica Sinica*, vol. 57, pp. 3593–3599, Jun. 2008.
[30] B. Sun *et al.*, "Photo-induced refractive index change of amorphous tin-doped As2S8 films and its application to strip waveguide fabrication," *J. Appl. Phys.*, vol. 105, May 1, 2009, Art. no. 094501.
[31] G. D. Wang, B. X. Chen, M. Iso, and H. Hamanaka, "Recovery process of optical stopping effect in tin or phosphorus-doped amorphous As2S8 thin-film waveguide," *Appl. Opt.*, vol. 51, pp. 4260–4264, Jun. 20, 2012.
[32] Z. Chen, G. D. Wang, X. Wang, and Q. Z. Zhao, "Moving toward optoelectronic logic circuits for visible light: A chalcogenide glass single-mode single-polarization optical waveguide switch," *Appl. Opt.*, vol. 56, pp. 1405–1412, Feb. 10, 2017.
[33] E. M. Izhikevich, "Class 1 neural excitability, conventional synapses, weakly connected networks, and mathematical foundations of pulse-coupled models," *IEEE Trans. Neural Netw.*, vol. 10, no. 3, pp. 499–507, May 1999.
[34] R. Eckhorn, H. J. Reitboeck, M. Arndt, and P. Dicke, "Feature linking via synchronization among distributed assemblies: Simulations of results from cat visual cortex," *Neural Comput.*, vol. 2, pp. 293–307, Sep. 1990.
[35] J. L. Johnson and M. L. Padgett, "PCNN models and applications," *IEEE Trans. Neural Netw.*, vol. 10, no. 3, pp. 480–498, May 1999.